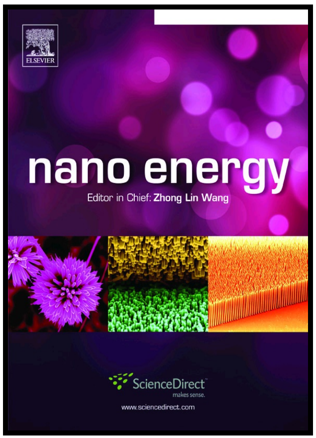
www.elsevier.com/locate/nanoenergy

Controllable Spatial Effect Acting on Photo-induced $CdS@CoP@SiO_2$ Ball-in-Ball Nano-photoreactor for Enhancing Hydrogen Evolution

He Li, Xiaoqing Yan, Bo Lin, Mengyang Xia, Jinjia Wei, Bolun Yang, Guidong Yang

PII: S2211-2855(18)30167-8
DOI: https://doi.org/10.1016/j.nanoen.2018.03.026
Reference: NANOEN2574

To appear in: *Nano Energy*

Received date: 9 January 2018
Revised date: 8 March 2018
Accepted date: 8 March 2018

Cite this article as: He Li, Xiaoqing Yan, Bo Lin, Mengyang Xia, Jinjia Wei, Bolun Yang and Guidong Yang, Controllable Spatial Effect Acting on Photo-induced $CdS@CoP@SiO_2$ Ball-in-Ball Nano-photoreactor for Enhancing Hydrogen Evolution, *Nano Energy,* https://doi.org/10.1016/j.nanoen.2018.03.026

Controllable Spatial Effect Acting on Photo-induced $CdS@CoP@SiO_2$ Ball-in-Ball Nano-photoreactor for Enhancing Hydrogen Evolution

He Li, Xiaoqing Yan, Bo Lin, Mengyang Xia, Jinjia Wei, Bolun Yang, Guidong Yang[*]

XJTU-Oxford Joint International Research Laboratory of Catalysis, School of Chemical Engineering and Technology, Xi'an Jiaotong University, Xi'an, Shaanxi 710049, China.

[*]Corresponding author. guidongyang@xjtu.edu.cn

Abstract

Size-controllable interior cavity of the ball-in-ball $CdS@CoP@SiO_2$ nano-photoreactor was fabricated using one-step hydrothermal method, Stöber method and combined with partially etching technique, and the size of inner-cavity can be precisely controlled with the different etching time. The experimental results show that the sample with a cavity diameter of 530 nm exhibits greatly higher photocatalytic activity and excellent stability compared with other sizes of inner-cavity samples and pure CdS@CoP sample, which could be attributed to its formed nanostructure properties, such as the proper inner-cavity distribution, visible light multi-scattering effect as well as reagent enrichment effect that confirmed by the NO removal reaction. However, noted that the ball in ball structure with interior cavity does not certainly improve the solar-driven hydrogen evolution under the visible light irradiation ($\lambda \geq 420$ nm), as is evident from the photocataytic activity of $CdS@CoP@SiO_2$ (CSC-1) with a cavity diameter of 450 nm shows the lower hydrogen evolution than pure CdS@CoP sample. These results exhibit that the size of the confined space plays a significant role in enhancing photocatalytic activity of the as-prepared nano-photoreactor. In addition, in order to further proof the function of the spatial cavity and the universality of this ball in ball nanostructure, we also prepared a series of referenced $CdS@SiO_2$ nano-photoreactor to validate again the spatial effect and apply in photocatalytic H_2 evolution (HER). As a result, the referenced photo-reactors also reveal the similar photocatalytic trend of HER activity, which aids the suitable size of spatial cavity indeed plays a crucial part in boosting photocatalytic H_2 generation and provides an innovative direction to further enhance HER activity. More importantly, exploring the factors over the different sizes of interior cavity can create a potential platform for designing the reasonable scale of the

nanoreactor applied in other fields and efficiently accelerate the conversion of reactants.

Graphical abstract

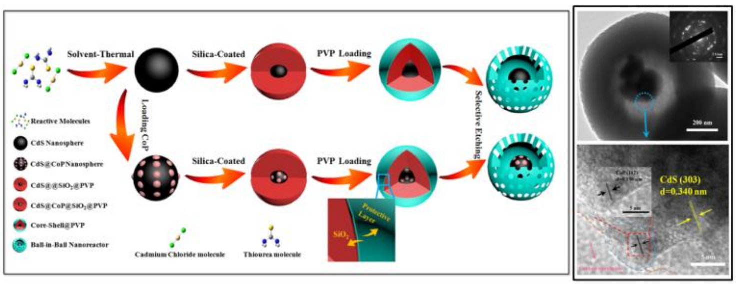

Keywords

Ball in ball, Photoreactor, CdS, CoP, Photocatalytic H_2 generation, NO removal

Introduction

Hollow nanostructured materials with tailored interior cavity and chemical properties provide excellent platforms for the catalysis, drug delivery, optics and energy storage [1-3]. The conventional hollow materials have derived series of complex nanostructures such as the yolk-shell, alveolus-like nanovesicle structure as well as ball-in-ball nanostructure in recent years [3-11]. Particularly, the generation of hydrogen from photocatalytic water splitting by utilizing the ball-in-ball nanostructure is anticipated a promising way to fabricate a low-cost, robust and sustainable photocatalyst in current years. Because this advanced ball-in-ball nanostructure with mesoporous shell, controllable internal cavity, spatial distribution and movable active core can act as aspecial photo-reactor to extremely improve the photocatalytic performance of semiconductors. For example, many literatures have been reported that the incident light can be scattered and redirected to various directions in the ball-in-ball nanoreactor that obviously enhancing the photo-absorption efficiency of the active center, as result of improving the conversion of positive photocatalytic reaction [12]. At the same time, the outer mesoporous shell can effectively prevent adhesion of the inner core during harsh conditions and highly increasing the stability of the whole system [3, 7, 17-19]. In addition, this kind of ball-in-ball nanostructure can utilize the internal void that extremely enriched the reactive molecules around the active centre so that leading to significantly enhance the photocatalytic activity by increasing the contact probability of the activated electron and reaction substrate.

Therefore, the special ball-in-ball photo-reactor has been attracted more attention of researchers and derived many series of synthetic methods to prepare this complex construction such as selective etching method, Ostwald ripening method, soft (surfactant) or hard (sacrificial layer) template method and ship-in-bottle method [6, 14]. For instance, Hu and co-workers have presented the coating colloidal carbon spheres with CdS (core-shell) photocatalyst to enhance HER activity. Shi and co-workers have reported the 3D-Array of Au-TiO_2 yolk-shell photocatalyst (1600 μmol g^{-1}) [12]. Lin and co-workers have fabricated g-C_3N_4@SiO_2 photo-reactor (176 μmol g^{-1}) to enhance hydrogen evolution [16], respectively. Although much more progresses have been achieved in recent years, the high-performance and stable ball in ball photocatalysts haven't obtained yet. This maybe because that above previous work only based on the multi-scattering effect and crystalline to design and synthesis the ball in ball structure, but whether the different sizes of the confined space in this nanostructure have any positive or negative influences acting on the catalytic activity, this relevant study is extremely limited [1, 20].

CdS as a narrow band (2.42 eV) of semiconductor exhibits remarked photo-induced activity, which can be served as one of optimal active core materials in ball-in-ball photo-reactors. While amorphous silica mostly being selected the outer shell material due to its highly translucent, stable and inexpensive properties. Nevertheless, the single inner core cannot availably enhance the hydrogen evolution, so co-catalytic ball-in-ball nanoreactors have been remarkably desired, which could strengthen the separation of electrons and holes for HER reaction. On the basis of above-mentioned analysis, in this work, we for the first time report the advanced CdS@CoP@SiO_2 ball-in-ball nano-photoreactor synthesized by the hydrothermal method combined with the modified Stöber method [10, 15, 21], then selectively etching the silica shell to obtain a series of materials with different interior cavity space and explore the influence of the different inner space sizes on their photocatalytic activity [13, 17, 22-25]. Meanwhile, we also fabricate CdS@SiO_2 ball in ball nanoreactor to further verify the effects of spatial structure on the photocatalytic performance. Additionally, by comparing the photocatalytic activity of these series of samples, which can clearly show that the space of interior cavity have a vital influence on the photo-absorption and reagents enrichment in the ball in ball structure. Meanwhile, the function of this nanostructure also can be as an ideal model for other catalytic system to improve the H_2-production from physical aspects.

Experimental section

2.1 Materials.

Cadmium chloride ($CdCl_2$, 99.99%), Thiourea (CH_4N_2S, 98%), polyvinylpyrrolidone (PVP, Mw≈40000.), Ethylene glycol (EG, 99.99%), ammonia solution (25-28%), 2-propanol (IPA, 99.99%), Tetraethylortosilicate (TEOS, 98%), Sodium hydroxide (NaOH, 99.99%), Cobalt acetate ($Co(CH_3COO)_2$, 99%), Sodium hypophosphite (NaH_2PO_2, 99%) were used without further purification.

2.2 Preparation of CdSNanospheres.

CdS nanospheres were synthesized using one-step hydrothermal method. The typical procedures were described as follows: 3.5 mmoL cadmium chloride, 10.5 mmoL thiourea and 1.2 g PVP (K30) was dissolved in a flask containing 40 mL ethylene glycol. The mixture was transferred to a 100 mL Teflon-lined stainless steel autoclave, which heated to 140^{o}C for 4 h. After cooling to nature temperature and washed with deionized water and ethanol for several times.

2.3 Preparation of CoP Nanoparticles.

The CoP nanoparticles were synthesized by the following method. Typically, 1.5 g $Co(CH_3COO)_2$ was dispersed in 20 mL 2-propanol with ultrasonic for 20 min, then 1 mL of ammonia solution was added in above system under magnetic stirring for 4 h. Afterward, the mixture was transferred into 100 mL Teflon-lined autoclave and kept at 160^{o}C for 4 h. The product was collected and washed with deionized water for several times, and dried at 60^{o}C for 3 h. Whereafter, the certain amount of the above Co_3O_4 was mixed with 2 g NaH_2PO_2 were heated at 300^{o}C for 2.5 h in N_2 atmosphere. At last, the resulted product CoP was collected.

2.4 Preparation of CdS@CoP Nanospheres.

The experimental process was adopted from the above method. First, 0.1 g CdS was dispersed in 20 mL 2-propanol. Subsequently, adding a certain amount of CoP solution (2 mg/mL) into the above solution under magnetic stirring for 3 h, and then the mixture was heated at 80^{o}C in water bath to remove the solvent. Briefly, the product was calcinated at 140^{o}C for 2 h and collected the final powder.

2.5 Preparation of CdS@CoP@SiO_2 core-shell Nanospheres.

The synthesis of CdS@CoP@SiO_2 core-shell nanospheres were carried out by the following modified Stöber method. Typically, 30 mL of 2-propanol, 1 mL of ammonia solution and 3 mL of deionized water were mixed and added 0.1 g of CdS@CoP in a flask. Then, 2 mL of TEOS was added rapidly and the mixture was vigorously stirred for 16 h at room temperature. Afterward, the products were washed several times with deionized water, and re-dispersed in 30 mL deionized water.

2.6 Preparation of CdS@CoP@SiO_2 Ball in Ball Photoreactor.

The above procedures were mixed with 1.0 g PVP (K30), and then refluxed for 5 h. When cooling the products down to room temperature, NaOH aqueous solution (5 mL, 0.2 g/mL) was added into the system to initiate etching. Then being etched for the 140 min, 165 min and 180 min, respectively, and then the products were collected by centrifugation and washed with deionized water and ethanol for several times. The obtained samples with different etching time of 140 min, 165 min and 180 min were denoted as CSC-1, CSC-2 and CSC-3, respectively.

2.7 Preparation of CdS@SiO_2 Ball in Ball Nanoreactor.

The CdS@SiO_2 ball in ball nanoreactor was synthesized by the same procedure described in the preparation of CdS@CoP@SiO_2 nanoreactor. Similarly, the obtained samples with different etching time of 140 min, 165 min and 180 min were denoted as CS-1, CS-2 and CS-3, respectively.

Characterization

The as-prepared samples were analyzed by various apparatus. The X-ray diffraction (XRD) patterns were analyzed by a powder X-ray diffraction (Lab X XRD-6100, SHIMADZU). The microstructure and morphology of the samples were observed by a transmission electron microscopy (JEM-2100, JEOL) and a scanning electron microscope (JSM-6700F, JEOL). The chemical elementary compositions of the products were obtained by the energy dispersive X-ray spectrometer. The properties of Ultraviolet-Visible (UV-vis) spectrum were measured by a UV-vis spectrophotometer (UV-2600, SHIMASZU). The photoluminescence spectra were recorded using a fluorescence spectrophotometer (QM-400, PTI). The in situ DRIFTS patterns were measured by a FTIR spectrometer (VERTEX70 Bruker) equipped with an in situ diffuse reflectance cell (Harrick). The DRIFTS spectra were determined using a scanning range of 4000-600 cm^{-1} with an average of 100 scans. Prior to measurements, the as-prepared samples were vacuum annealed at 150℃ in He to remove the CO_2, H_2O and other gas molecules before the experiment. After the samples were cool down to the room temperature, the gas mixture (60 ppm NO and 10% O_2 in He, 25 mL/min) pass through the reactive system. Both of the NO removal experiment and NO adsorption were tested under the same flow. The surface photovoltage spectrum was measured by a solid junction apparatus with a light source-monochromator-lock-in detection measurement. And the monochromatic light was acquired with the 500-W xenon lamp through a triple-prism monochromator (Hilger and Watt, D300). An amplifier (Brookdeal, 9503-SC) synchronized with a light chopper was obtained to amplify the signal of photovoltage. All the spectra were normalized to unity at the feature peaks of the xenon lamp were detected by a computer. The whole SPS tests were performed at room temperature with an ITO electrode film (photoabsorption below 340 nm). The principle and schematic diagram of the SPS apparatus were described in detail elsewhere [26, 27].

Photocatalytic hydrogen evolution

The H_2 production was tested on in the glass reactor at room temperature for irradiation experiments with the visible-light ($\lambda \geq 420$nm). Briefly, 0.02 g of photocatalyst dissolved in the 50 mL deionized water that containing 5 mL lactic acid (sacrificial electron donor) as a sacrificial reagent. Then the solution was degassed with N_2 for 20 min to drive away the O_2 in the solution, the reaction vessel was exposed to the visible light irradiation. Then the H_2-production was evaluated by a gas chromatograph (SP-2100A, Beifen-Ruili) with thermal conductivity detection and the catalytic reaction carried out under the illumination of a 300W Xenon lamp (HSX-F300, Nbet Beijing) equipped with a 420 nm cutoff filter.

The stability tests of the photocatalytic activity of the series of samples (CdS, CdS@CoP, CS-2 and CSC-2) were carried out under the same reaction condition to explore the durability and sustainable properties. The cycle experiment was investigated for 16 h, after every 4 h photoreaction, the photocatalyst was separated from the original reaction system by centrifuation (10000 rpm), and washed by deionized water and ethanol for several times. then dried in a drying oven for 5 h at 60℃. The dried sample and the same volume of aqueous solution (50 mL deionized water) with 5 mL sacrificial reagent (lactic acid) were adding into 100 mL reaction vessel, respectively. Prior to the photoreaction, the system was bubbled with N_2 for 20 min to remove away the O_2 in the reaction solution.

Besides, using the monochromatic light (435 nm, 750 uW/cm^2) as a light source. Subsequently, the average hydrogen evolution rate was detected after irradiated for 2 h. That is, the quantum efficiency was calculated by the following equation.

The apparent quantum yield (AQY%) for the as-prepared samples were measure by monochromatic light (λ=435 nm, 750 uW/cm^2) as a light source, the average hydrogen evolution rate was detected after irradiation for 2 h. And AQY(%) was calculated by the following equation [27-30]:

$$\begin{aligned} \text{AQY (\%)} &= \frac{\text{Number of reactor electrons}}{\text{number of incident photons}} \times 100 \\ &= \frac{2 \times \text{nunber of evolved hydrogen molecules}}{\text{number of incident photons}} \times 100 \end{aligned}$$

Photoelectrochemical measurement

The electrochemical impedance spectra and photocurrent response of the as-synthesized samples were detected by a CHI 660D type electrochemical station (Chenhua China) and a PMC-1000/DC type one (AMETEK), respectively. Both of the tests are in the same three-electrode system. We choose the platinum wire and Ag/AgCl electrode platinum wire as the counter electrode, reference electrode and the glassy carbon electrodes loading with as-prepared samples were regarded as the working electron in this system, respectively.

Results and discussion

High photocatalytic activity of H_2-production

The overall synthesis process of CdS@CoP@SiO_2 is primarily presented in Fig. 1. Firstly, the pure CdS nanospheres were synthesized by one-pot hydrothermal method and then the heat treatment method was applied to synthesize CdS@CoP nanospheres. Afterwards, relied on the modified Stöber method, the SiO_2 outer shell can be easily coated on the surface of CdS@CoP nanospheres under alkaline condition. Secondly, the above predecessor was absorbed and loaded with certain molar of PVP under 100°C for 5 h. After that, sodium hydrogen solution (5 M) was used to selectively etch the shell from inside to outside owing to the protection of PVP, the core-shell structure was therefore conveniently convert into ball-in-ball CdS@CoP@SiO_2 nanostructure. Finally, through changing the etching time, a series of CdS@CoP@SiO_2 ball-in-ball photo-reactor with different interior cavity space between core and shell was synthesized. In addition, we also fabricate the series of CdS@SiO_2 photoreactor in the same process for comparison.

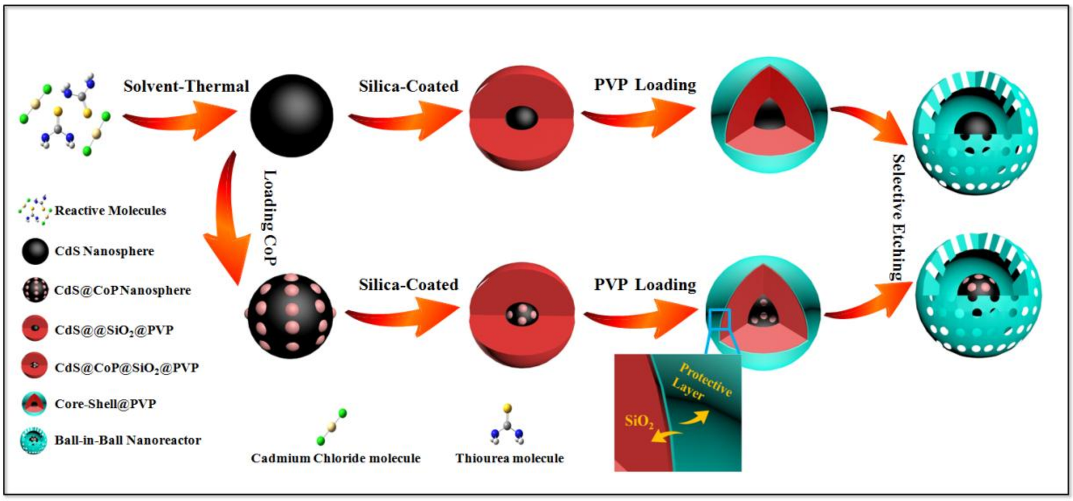

Fig.1. Schematic representative of the formation procedure for ball-in-ball nano-photoreactors.

To illustrate the photocatalytic effectiveness of special ball in ball nano-photoreactor, the photocatalytic hydrogen-evolution rate (HER) over the as-prepared samples were examined in 5 vol.% lactic acid aqueous solution under visible-light irradiation (λ≥420nm). Notably, it can be seen from the Fig. 2a that the pristine CdS@CoP shows a relatively low photocatalytic H_2-production of 32400 μmol g^{-1} within 4 h photoreaction. In comparison, the CSC-2 sample exhibits the highest HER activity of 70910 μmol g^{-1}, exceeding that of the pristine CdS@CoP by a surprise factor of 2.19. And the CSC-3 sample with the HER activity of 49070 μmol g^{-1} is slightly higher than that of the pristine CdS@CoP. Interesting, the CSC-1 sample shows lower HER performance of 17470 μmol g^{-1}, which is lower than that of pristine CdS@CoP. Based on the above solar-driven H_2-production experimental data, it can be seen that the CSC-2 sample exhibits the highest photocatalytic activity despite its internal space is not the largest in comparison with the other two samples. In addition, the quantum efficiency of the CSC-2 sample is also calculated to be 23.6%, which is much higher than that of the pristine CdS@CoP (17.8%).

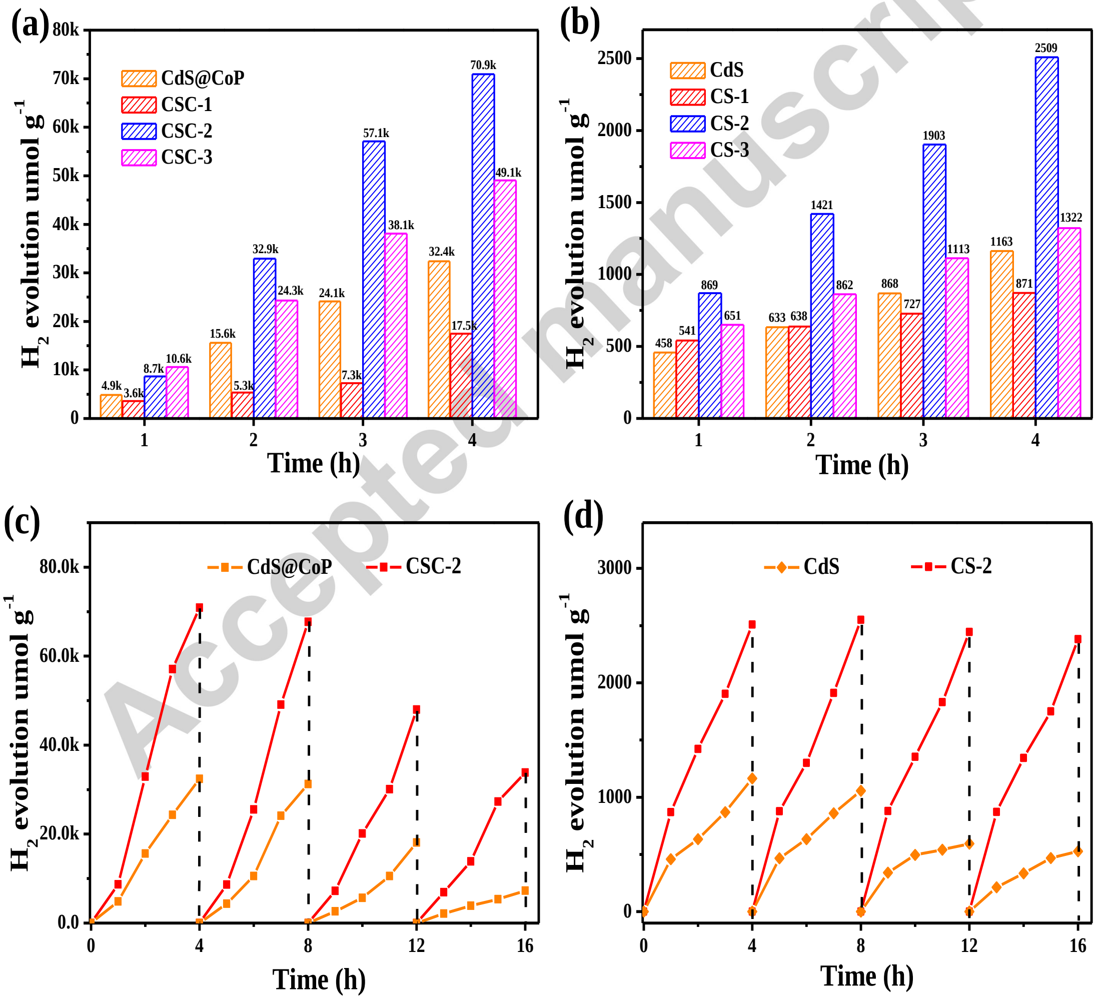

Fig. 2. (a) Time-dependent solar-driven H_2 evolution for different as-synthesized CdS@CoP@SiO_2 nanoreactorsunder under visible-light irradiation (λ≥420 nm). (b) Time-dependent solar-driven H_2 evolution for CdS@SiO_2 nanoreactorsunder under visible-light

irradiation (λ≥420 nm). (c) Cycling runs experiments of photocatalytic hydrogen evolution for CSC-2 and CdS@CoP. (d) Cycling runs experiments of photocatalytic hydrogen evolution for CS-2 and pristine CdS under visible-light irradiation (λ≥420 nm).

Additionally, in order to further prove the advantages of the confined cavity for the photo-induced reaction, the photocatalytic properties of CdS@SiO_2 nanoreactors were tested under the same condition. Wondrously, this kind of CdS@SiO_2 samples shows the similar activity trend with the CdS@CoP@SiO_2 ball-in-ball photo-reactor. As shown in Fig 2c, the CS-2 shows H_2-production of 2509 μmol g^{-1}, which exceeds that of CdS (1163 μmol g^{-1}) by a factor of 2.16. The CS-1 exhibits the lowest H_2 generation (871μmol g^{-1}) among these as-synthesized samples. Similarly, in the series of CdS@SiO_2 nanoreactor samples, the CS-2 also shows the highest quantum efficiency (16.6%), which is slightly exceeding the pure CdS (13.1%). From the above experimental results, it is imperative to realize that internal confined space certainly take a significant influence on the interfacial redox reaction and the efficiency of capturing photons, facilitating the improvement of the solar-driver photocatalytic hydrogen production.

Moreover, the photocatalytic stability of pristine CdS@CoP nanospheres and the optimized CSC-2 sample are detected under the same experimental conditions [31,32,35,37]. As shown in Fig. 2b, there is marked decline (from 70910 μmol g^{-1} to 33850 μmol g^{-1}) of photocatalytic activity was measured over the optimized CSC-2 sample after the four times cyclic test. Likewise, the CdS@CoP sample also represents the significant HER drop from 32400 μmol g^{-1} to 7260 μmol g^{-1}. After photocatalytic cycling run tests, the XRD pattern of the used CdS@CoP and CSC-2 both show the presence of additional peak at 53.11° in Fig. S1a (Supporting Information), which can be corresponded to CoP_3 (JCPDS NO. 29-0496), suggesting that the instability of the as-prepared CSC-2 samples might derive from the random loaded CoP NPs being decomposed to CoP_3 during the continuous cycle tests. Fortunately, Fig. 2d shows that the CS-2 photo-reactor has excellent stability during the fourth cyclic test, and the pure CdS nanospheres exhibit the marked HER decline from 1163 μmol g^{-1} to 527 μmol g^{-1} due to the photo corrosion effect of CdS. While the SEM images in Fig. S2 (Supporting Information) show that after cycling runs tests the pristine CdS and CdS@CoP nanospheres have a serious aggregation and cross-linked phenomenon, but the ball-in-ball nanostructure efficiently hinders the reuniting of CdS nanospheres during the photoreaction. These results from another aspect proof that the suitable interior cavity in some degree provides a stable and homogeneous environment to prevent photo-corrosion and catalyst reunite during the reaction.

The Chemical composition and structure of the photocatalyst

Fig. 3a shows the X-ray diffraction (XRD) patterns of the series of CdS@SiO_2 photo-reactors. Seven main characteristic peaks can be obviously observed in the XRD data of pure CdS, CS-1, CS-2 and CS-3 at 24.7°, 26.6°, 28.3°, 36.8°, 43.7° 48.1° and 52.1° corresponding to the (400), (330), (240), (053), (444), (722) and (080) diffraction plane of the orthorhombic structure CdS (JCPDS NO. 47-1179), respectively. Furthermore, the lattice spacing of 0.340 nm observed by HRTEM (Fig. 6b) can be assigned to (303) plane of pure CdS (a=14.315Ǻ, b=14.074Ǻ, c=14.568Ǻ) [33-35]. These data can highlight the well crystallinity of the CdS core in the photo-reactors. Fig. 3b shows the XRD patterns of the CdS@CoP@SiO_2 products. As shown, except the characteristic peaks of CdS, four typical peaks could be explicitly observed at 32.0°, 36.7°, 48.1° and 52.3°, which can be indexed to the (002), (102), (211) and (103) crystal plane of CoP (JCPDS NO. 29-0497), suggesting that the CoP co-catalysts have been successfully coated on the skeleton of CdS nanosphere. In addition, a weak and broad peak located at around 23° can be assigned to the amorphous silica shell existed in both the CdS@SiO_2 and CdS@CoP@SiO_2 nanoreactor.

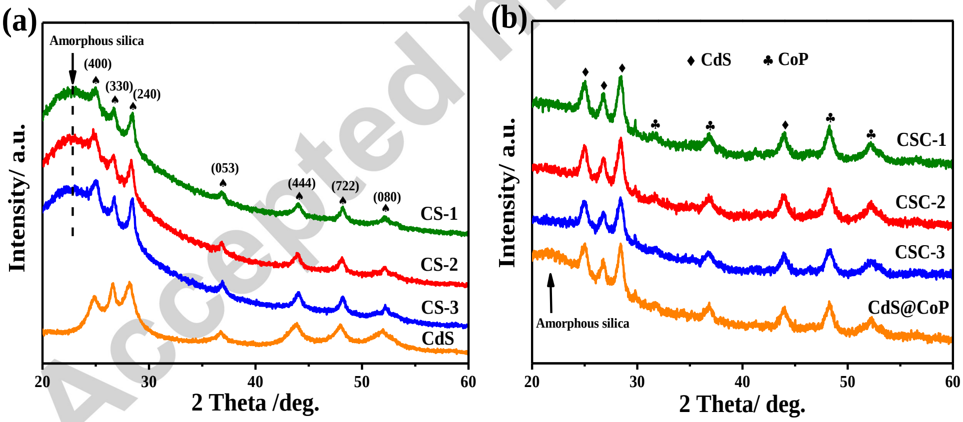

Fig. 3. The XRD patterns of (a) as-synthesized CdS@SiO_2 and (b) CdS@CoP@SiO_2 samples.

Fig. S3 (Supporting Information) shows the SEM and TEM images of the pristine CdS and CdS@CoP samples. As can be seen from Fig. S3 (a, b) pure CdS presents the cauliflower-like nanosphere with the smooth surface and the average diameter of the individual CdS nanosphere is about 230 nm. Additionally, CdS@CoP has obvious rough surface compared with pure CdS nanospheres and several CoP NPs loaded on the surface of CdS nanospheres can be clearly observed. (Fig. S3 (c, d), Supporting Information).

Fig 4 a-c show the SEM images of the obtained CdS@SiO_2 photo-reactor samples. It can be seen that the series of the CdS@SiO_2 samples exhibit the typically spherical morphology and the bright core of CdS nanosphere with average diameters of 230 nm was observed. Additionally, it can be seen that, as the cavity size increases, the core becomes more clear and bright. Fig 4 d-f show the TEM images of the individual CS-1, CS-2 and CS-3 ball in ball samples. It can be clearly observed that CS-1 is consisted of a cauliflower-like core with the average of 450 nm diameters inner cavity and the average 270 nm outer shell. The CS-2 has the average 530 nm diameters inner space and the average 200 nm shell, while the CS-3 is composed of the average 610 nm diameters of spatial cavity and the average 140 nm of outer shell. Specially, the corresponding EDX elemental mapping tests are displayed in Fig. S4 (Supporting Information), which confirms that the CS-2 composite sample contained the elements of oxygen (O), cadmium (Cd) and sulfur (S), this is consistent with XRD data.

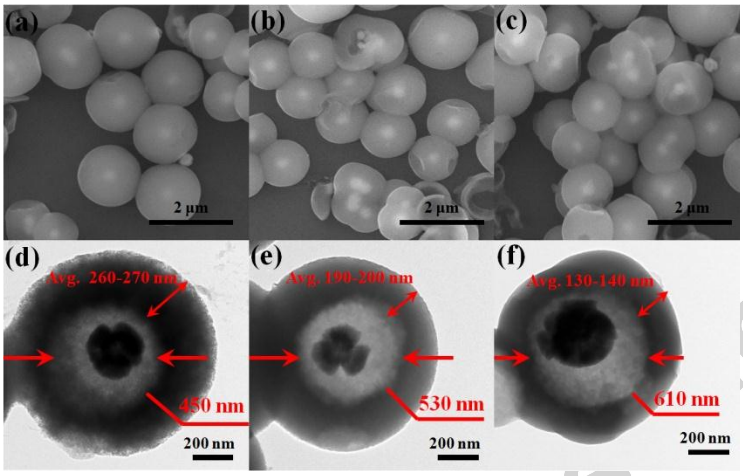

Fig. 4. SEMand TEM images of (a, d) CS-1, (b, e) CS-2 and (c, f) CS-3.

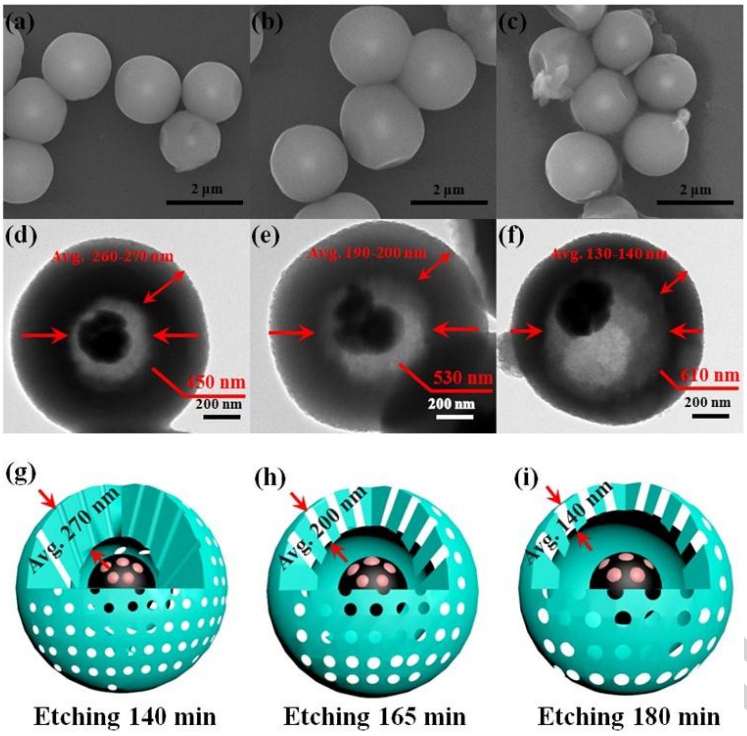

Fig. 5. SEM and TEM images of (a, d) CSC-1, (b, e) CSC-2 and (c, f) CSC-3 and their schematic diagrams.

Fig. 5 a-c show the SEM images of the CdS@CoP@SiO$_2$ photo-reactor products. As shown, a typical spherical morphology (average of 1.6 μm diameter) with a bright core for the target photocatalyst can be observed, like the above-mentioned CdS@SiO$_2$ photo-reactor samples. Fig. 5d-f clearly show CSC-1 has the average diameter of 450 nm spatial cavity and about 270 nm outer shell. As for CSC-2, it is obvious that the CSC-2 has the average diameter of 530 nm confined space and the average 200 nm outer shell, while the obtained CSC-3 possesses the average of 610 nm diameter and approximately 140 nm outer shell. Based on the TEM and SEM results, the formed confined space size and shell thickness of the ball-in-ball CdS@CoP@SiO$_2$ photo-reactor can be clearly demonstrated by model figures (Fig. 5 g-i). In addition, it is noted that the use of silica as the outer shell not only can cause the reagent enrichment effect and strengthen visible-harvesting capability of CdS@CoP due to its relative transparent property, also can provide a protective shell that prolonged the service life of the main catalyst.

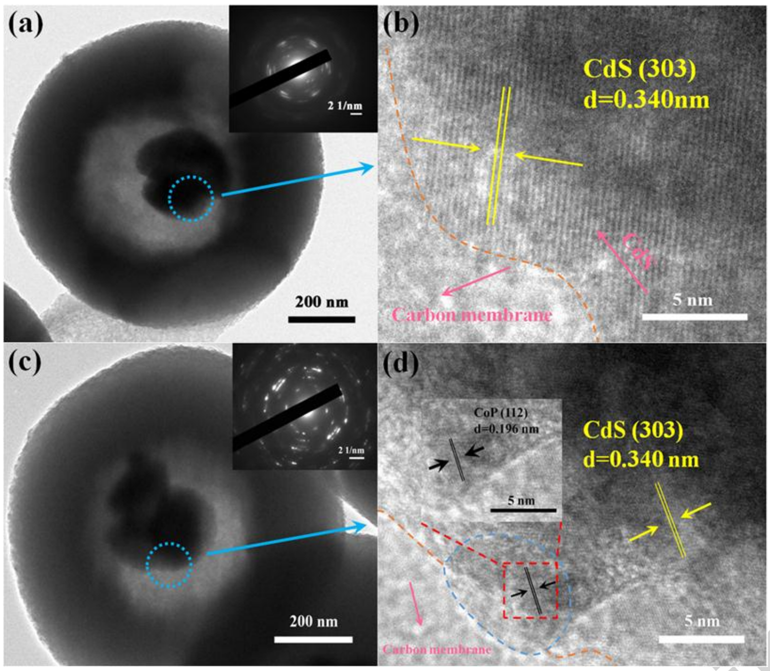

Fig. 6. (a) The TEM images of CS-2 (SAED pattern insect), (b) The high-resolution TEM image of CS-2, (c) The TEM image of CSC-2 (SAED pattern insect), (d)The high-resolution TEM image of CSC-2.

Subsequently, the typical high-resolution TEM (HRTEM) images in Fig. 6 (a, b) reveal that a cauliflower-like CdS served as a core in the inner cavity, and the lattice space of 0.340 nm corresponds to (303) crystal plane of orthorhombic CdS, indicating the successful synthesis of CdS@SiO_2 photo-reactor samples. And then the selected area electron diffraction image (the inset of Fig. 6a) exhibits the cauliflower-like CdS core has the excellent crystallinity. In Fig. 6 (c, d), the individual CSC-2 sphere shows the clear lattice spaces of 0.340 nm and 0.196 nm can be matched to (303) plane of orthorhombic CdS and (112) plane of orthorhombic CoP. With its corresponding selected area electron diffraction image (the inset of Fig. 6c), both confirm that the presence of well-defined orthorhombic CdS and CoP nanocrystals in the ball-in-ball CdS@CoP@SiO_2 photo-reactor.

Light-harvesting capability

Fig. 7 shows the light-harvesting capability of the as-synthesized samples, which elucidated by the ultraviolet-visible diffuse reflectance spectra. As shown in Fig. 7a, the light absorption of the optimized sample CSC-2 is obviously increased in the visible-light region of 490-620 nm among these as-formed samples. This result is ascribed to the fact that the multi-scattering effect produced by the proper interior cavity space of ball in ball structure substantially boosts the visible light absorption [12, 15, 34]. To carefully observe the UV-vis spectra, it can be seen that the optical absorption ability along the increase of interior cavity presents a gradient distribution.

More significantly, the visible-light harvesting of the CSC-3 is higher than CSC-2 in the range of 420-490 nm. And the CSC-1 shows the lowest visible-light harvesting in range of 420-600 nm but is higher than that of CdS@CoP in range of 470-600 nm. Not surprisingly, it can be observed in Fig 7b, the Cd@SiO_2 photo-reactors reveal similar optical properties, CS-3 shows slightly stronger light absorption among the as-prepared samples in range of 475-550 nm. Additionally, CS-2 has the strongest visible-light harvest in range of 550-600 nm and CS-1 shows the lowest visible-light harvesting among the obtained ball in ball Cd@SiO_2 samples. As is evident from these data, the different volume of void space indeed affects the optical properties, which aiding charge separation and enhancing photoreaction.

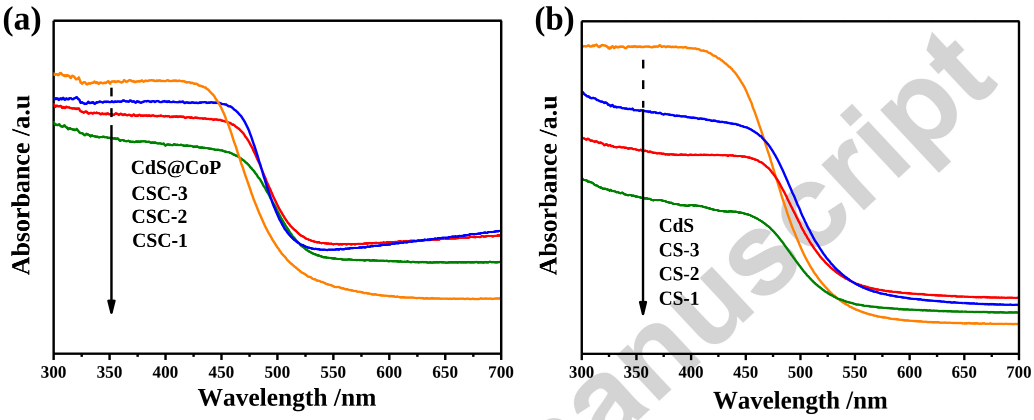

Fig. 7. The UV-vis diffuse spectra for (a) CdS@CoP@SiO_2 and (b) CdS@SiO_2 samples.

The Charge transfer and Separation performance of photocatalysts

To further reveal the surplus photocatalytic activity of the optimized sample. The PEC analysis was used to comprehensively elucidate the efficiency of charge transfer and separation under the intermittent visible light condition ($\lambda \geq 420$ nm) in this system. And the curves of transient photocurrent-time (I-t) recorded for CdS@CoP@SiO_2 samples (Cd@CoP, CSC-1, CSC-2 and CSC-3) are displayed in Fig. 8a, it is obvious

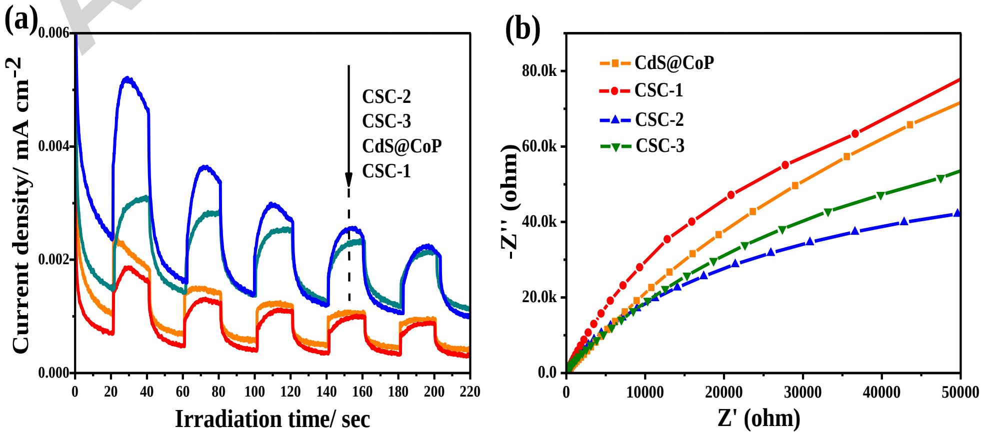

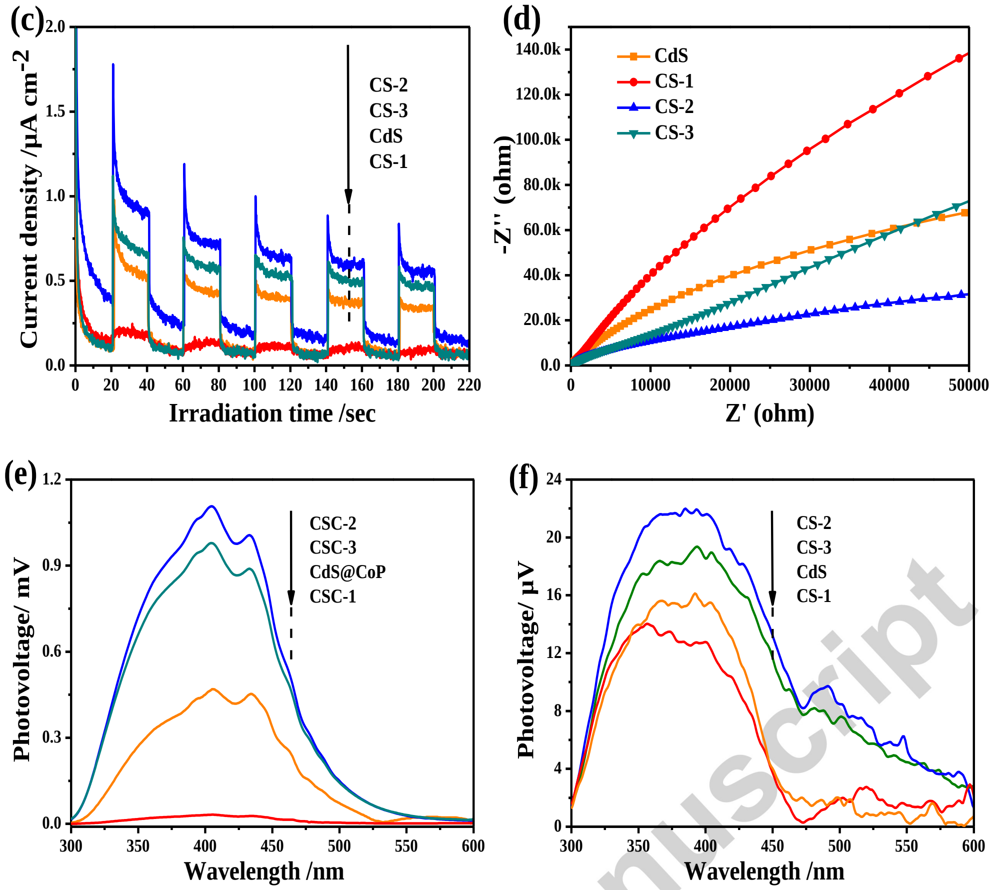

Fig. 8. (a) Transient photocurrent responses spectra and (b) EIS Nuquist plots for CdS@CoP@SiO$_2$ nanreactor samples. (c) Transient photocurrent responses spectra and (d) EIS Nuquist plots for CdS@SiO$_2$ nanoreactor samples. The Surface photovoltaic spectrum of (e) CdS@CoP@SiO$_2$ photo-reactors and (f) CdS@SiO$_2$ photo-reactors.

that the optimized CSC-2 represents the highest photocurrent density compared with CdS@CoP, CSC-1 and CSC-3 samples, which evidently demonstrates the inner void structure can remarkably enhance the interfacial transfer and separation of the photo-generated electron-hole pairs, therefore directly contributing the solar-driven activity. However, we can clearly observe the decline of photocurrent density with time going by, this phenomenon matched the stability measurement result owing to the loaded CoP cocatalyst being decomposed to CoP$_3$ and thus caused the attenuation of charges separation ability. Accordingly, in the Fig 8c, the electrochemical responses of the series of CdS@SiO$_2$ samples (CdS, CS-1, CS-2 and CS-3) totally fitted the above experimental phenomenon. Not excitingly, CS-2 with a diameter 530 nm interior space also shows the highest photocurrent density than other samples, which firmly confirming the suitable spatial effect can accelerate the migration rate of photo-generated charges and improve their separation and transfer during the photocatalytic process. In addition, the spectra of electrochemical impedance spectroscopy (EIS) were also measured in the dark condition. As shown in Fig. 8b, the EIS Nyquist plots of CSC-2 photocatalyst exhibits the extremely smaller arc radius than CdS@CoP, CSC-1 and CSC-3 samples, respectively. Meanwhile CSC-1 shows the biggest arc radius in the four samples and CSC-3 has the middle arc radius between the CSC-2 and CdS@CoP. With respect to the series of CdS@SiO_2 ball in ball nanoreactor, the tendency of EIS Nyquist is similar with CdS@CoP@SiO_2 ball in ball nanoreactor (Fig 8d). The CS-2 exhibits the minimum arc radius in the series of products, which further proves the previous conclusion [3, 9]. And CS-1 has the maximum arc radius among these samples, meanwhile CS-3 matches the results of HER activity that has larger arc radius than CS-2.

To further confirm the improvement of the charge separation rate, the surface photovoltaic spectrum (SPS) techniques was adopted to further reveal the interfacial charge migration of the as-synthesized samples. Fig. 8 (e, f) show the SPS response of the as-prepared photo-reactor samples, based on the mechanism of SPS, the photovoltaic response intensity is relative to its degree of electrons and holes separation. To be extended, the stronger the SPS signal is, the easier the charges separation. Thus, Fig. 8e reveals the CSC-2 has the strongest response in these as-prepared samples, and then the CSC-3, CdS@CoP and CSC-1 decreased in the wave number of 300-600 nm in turn. This is due to the fact that CdS@CoP@SiO_2 samples with the different sizes of inner space show different optical absorption, which directly affect the capability of charges separation during the SPS tests, so that ultimately causing the improvement of HER activity [36]. With respect to CdS@SiO_2 nanoreactors, CS-2 gives the greatest surface photovoltaic response among the samples in the wavelength range of 300-600 nm (Fig 8f). Next, the photovoltage of CS-3 exceeds the pristine CdS and CS-1 perfectly matches the tendency of CdS@CoP@SiO_2 nanoreactors.

Specially, the transient fluorescence decay spectra for the optimized CS-2, CSC-2 pure CdS and CdS@CoP were tested as shown in Fig. 9. And the fitting kinetic parameters (including the relative amplitudes and two radiative lifetimes) were summarized in insect table of Fig 9. The fluorescence intensities of CSC-2 and CdS@CoP are accorded with double-exponential decay kinetics in Fig. 9b. That is, the short lifetime (τ_1) of charge carriers decreases from 0.48 ns (CSC-2) to 0.38 ns (CdS@CoP), subsequently the long lifetime (τ_2) of charge carries distinctly increases from 3.70 ns (CdS@CoP) to 4.44 ns (CSC-2). With respect to pure CdS and CS-2 that the short lifetime (τ_1) of charge carriers decreases from 0.82 ns (CS-2) to 0.66 ns (CdS nanospheres), but the long lifetime (τ_2) of charge carries remarkably increases from 10.28 ns (CdS nanospheres) to 11.01 ns (CS-2) in Fig. 9a. As is evident from the above experimental result can illustrate both the optimal cocatalytic CSC-2 and the CS-2 can prolong radiative lifetime of charge carries which contributed by the suitable inner cavity in notable ball-in-ball nano-photoreactor [28]. Notably, it can be clearly seen that the fluorescence intensity of CS-2 is longer than CSC-2, this experimental result mainly based on using the different emission wavelength CdS and CS-2 (640 nm) but CdS@CoP and CSC-2 (683 nm) during the transient fluorescence test. Thus the fluorescence decay spectra for series of CdS and CS-2 cannot compare with CdS@CoP and CSC-2. Even though, we can distinctly observe ball-in-ball photo-reactor certainly improving the fluorescence response due to spatial effect.

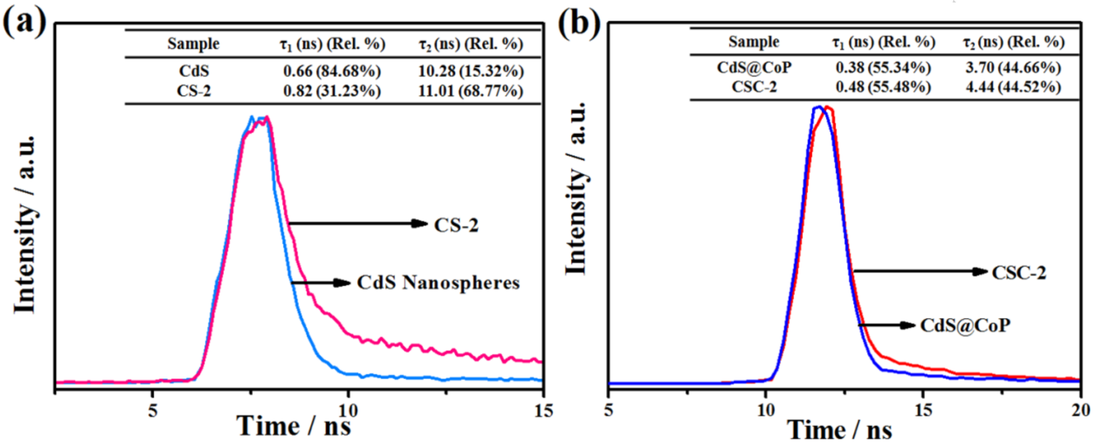

Sample	τ_1 (ns) (Rel. %)	τ_2 (ns) (Rel. %)
CdS	0.66 (84.68%)	10.28 (15.32%)
CS-2	0.82 (31.23%)	11.01 (68.77%)

Sample	τ_1 (ns) (Rel. %)	τ_2 (ns) (Rel. %)
CdS@CoP	0.38 (55.34%)	3.70 (44.66%)
CSC-2	0.48 (55.48%)	4.44 (44.52%)

Fig. 9. Transient fluorescence decay spectra for (a) CdS@SiO$_2$ nanoreactors (emission wavelength at 640 nm) and (b) CdS@CoP@SiO$_2$ nanoreactors (emission wavelength at 683 nm).

The NO adsorption and removal performance of photocatalysts

Fig. 10 (a, b) represent the spectra of photocatalytic NO removal over the as-synthesized samples under visible light irradiation (λ≥420 nm). After about 6 min irradiation the NO removal rate of CSC-2 (25.8%) is extraordinary higher than that of

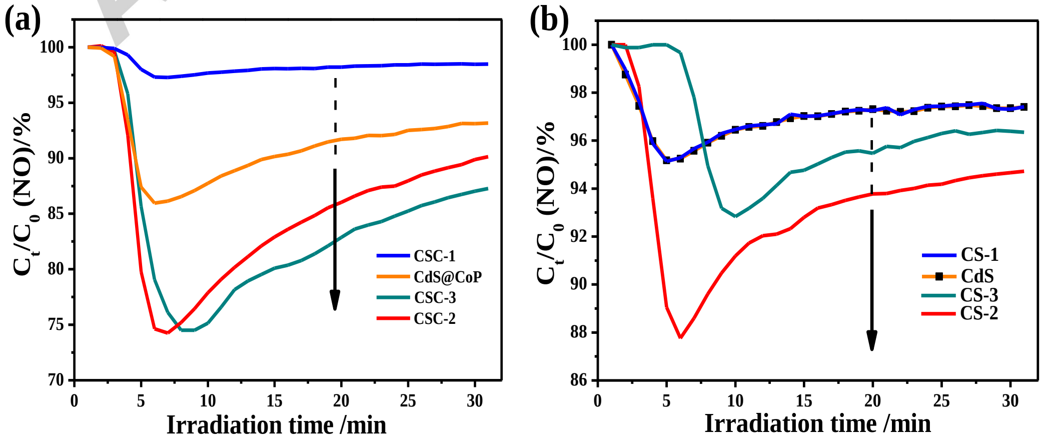

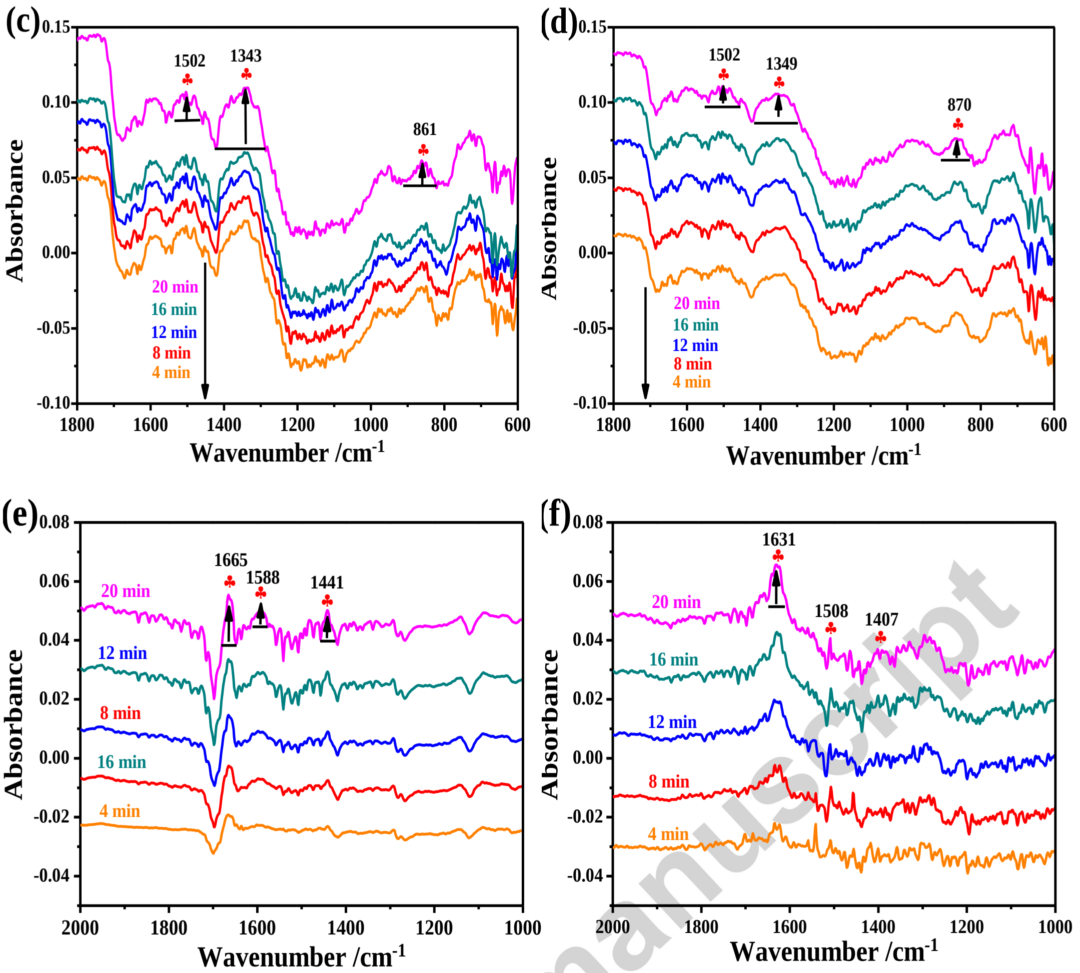

Fig. 10. Solar-driven NO removal performance for (a) CdS@CoP@SiO_2nanoreactorsmaples and (b) CdS@SiO_2 nanoreactorsmaples. In situ IR spectra of NO adsorption over (c) CSC-2, (d) CdS@CoP, (e) CS-2 and (f) pristine CdS under a flow of 60 ppm NO +10% O_2 in He.

CdS@CoP (14.1%), powerfully proving that the interior cavity structure exactly promotes redox reaction (Fig. 10a). Notably, with the sizes of interior cavity changing, CSC-2 exhibits the highest NO removal rate than that of CSC-1 (2.8%) and CS-3 (25.5%), indicating that the CdS@CoP@SiO_2 sample with interior cavity sizes of 530 nm is the optimal value for the NO removal. Fig 10b represents CS-2 has the optimal NO removal rate (13.3%). And CS-1 and pure CdS show approximate activity of 4.9% NO removal. Moreover, as shown in Fig. S1b (supporting Information), it can be clearly seen that the characteristic peaks of CoP located at 32.0°, 36.7°, 48.1° and 52.3°, which can be indexed to the (002), (102), (211) and (103) crystal plane of CoP (JCPDS NO. 29-0497). But after NO removal reaction, the characteristic peak located at 32.0° has disappeared, which can certainly elucidate the CoP was decomposed. This phenomenon illustrated CoP has the poor stability during the NO removal reaction. In addition, Fig. S1c (supporting Information) reveals the main characteristic peaks of CS-2 sample were never changed due to the construction of photo-reactor has a protective effect on active core. Above experimental data also perfectly matched the data of recycled experiment for H_2 generation of CSC-2 and CS-2 samples, which further confirmed the ball-in-ball structure could enhance the stability of CdS.

In order to explore the function of confined space during the redox reaction process, the in situ DRIFTS tests of the above samples were detected under the same condition. Fig. S5 (Supporting Information) shows the time dependence of the IR spectra for the NO removal process of the CSC-2, CdS@CoP, CS-2 and CdS, respectively. It can be clearly seen in Fig. S5a, the IR absorption peaks of CSC-2 at 1334 cm^{-1} (nitro species), 1452 cm^{-1} (nitro species), 1576 cm^{-1} (monodentate NO_3^-), and 1641 cm^{-1} (NO_3^-) confirmed that NO molecules can availably oxidize to high-priced compounds during redox reaction. In comparison with CSC-2 sample, although the main IR absorption peaks of nitro species (1336 cm^{-1}), nitro species (1451 cm^{-1}), monodentate NO_3^- (1598 cm^{-1}) and NO_3^- (1659 cm^{-1}) remain in the obtained CdS@CoP sample with increase of the reaction time, their intensity were significantly lower than CSC-2 (Fig. S5b), indicating a lower activity of NO removal.

Subsequently, Fig. S5 c,d (Supporting Information) represent the in situ IR spectra of NO removal process for the CS-2 and CdS. The characteristic IR absorption peaks of CS-2 at 1022 cm^{-1} (bidentate NO_3^-), 1118 cm^{-1} (NO^-), 1243 cm^{-1} (bidentate NO^-), 1400 cm^{-1} (nitro species), 1598 cm^{-1} (monodentate NO_3^-) and 1722 cm^{-1} (N_2O_4) were clearly detected in Fig. S5c [37, 38]. Meanwhile, the intensities of above the characteristic peaks remarkably increase with the irradiation time going by. With respect to the pristine CdS, only the 1118 cm^{-1} (NO^-), and 1307 cm^{-1} (nitro species) can be recorded in Fig. S5d and displays a negligibly intensity change of the two characteristic peaks during NO removal experiment, which further indicating that pristine CdS nanospheres exhibits the lower activity in comparison with CS-2. These results evidenced that the inner cavity is beneficial to diffuse and absorb the NO and O_2 molecules accordingly to promote the redox activity.

Furthermore, the intensification of NO adsorption process can be, further confirmed by the in-situ absorption IR spectra. As shown in Fig. 10 (c, d), it can be clearly found that there are several distinct peaks at 861 cm^{-1} (nitro species), 1343 cm^{-1} (NO) and 1502 cm^{-1} (NO_3^-) appeared in the CSC-2, while these peaks of nitro species, NO and NO_3^- species also observed in IR spectrum of CdS@CoP. However, after 20 min absorption, the results of in situ IR spectra show that the intensity of these characteristic peaks in CSC-2 were much higher than that in CdS@CoP. In addition, the similar phenomenon is also occurred in the CdS@SiO_2 nanoreactor sample. As shown in Fig. 10e, the characteristic peaks at 1441 cm^{-1} (nitro species), 1588 cm^{-1} (monoderate NO_3^-) and 1665 cm^{-1} (nitro species) can be clearly observed in both the IR spectrum of CS-2 and pure CdS nanospheres. And it is clear that the intensities of these peaks for CS-2 is higher than that of pristine CdS (Fig. 10f), indicating the nano-photoreactor structure indeed enhances the enrichment of NO molecules inside the interior cavity and thus improves the redox performance [16, 39]. These robust evidence can prove that the enhanced NO removal rate mainly relies on advanced ball-in-ball nanostructure and the spatial confinement is beneficial to enrich the gas molecules during the gas-solid reaction system.

Visible-light-driven H_2 production mechanism and discussion

As the aforementioned analysis, it is obvious that the different spatial cavity of photo-reactors certainly raises the different properties of optical and mass transfer during the photo-induced reaction. Thus, from the reaction mechanism diagram in Fig. 11, we try our best to reveal the effect of reagent enrichment and multi-scattering on the enhancement of HER activity and NO removal rate in the interior cavity of ball in ball photoreactor.

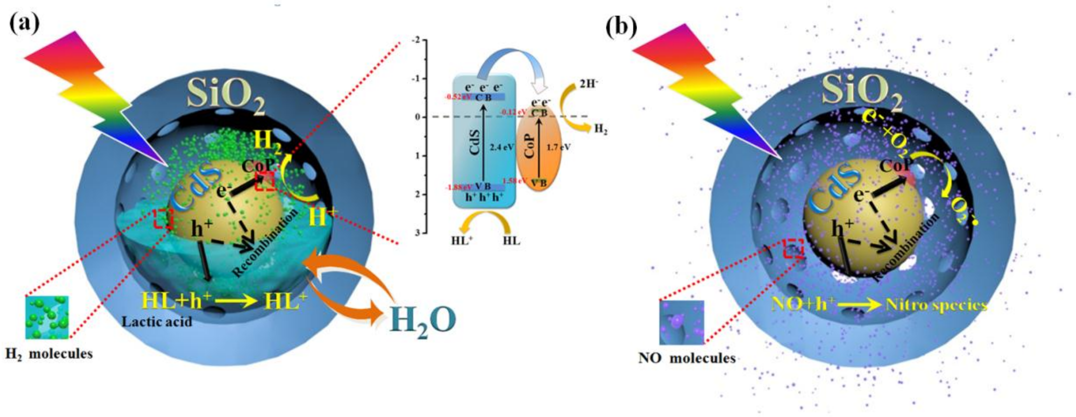

Fig. 11. Proposed mechanism of solar-driven hydrogen evolution and NO removal reaction over ball-in-ball nano-photoreactor under visible light irradiation (λ≥420 nm).

The TEM results have clearly shown that the CSC-1 sample has the thickest outer shell and narrow interior cavity. When the visible light beginning to irradiate, most of the incident light can be easily consumed and diffused to pass through the long channel in the mesoporous outer shell, so that a very limited amount of light can be utilized by CdS@CoP core in CSC-1. This can be supported from the UV-vis spectra, CSC-1 exhibits the lowest light absorption thoroughly the 300-600 nm wavelength compared with CSC-2 and CSC-3 [12, 34, 40]. Not surprisingly, the referenced CS-1 sample also has the worst light absorption during the 300-600 nm wavelength in photo-reactor samples due to the same reason above discussed. As a result, both the CSC-1 and CS-1 similarly show the lowest photocurrent densities and the largest arc radius, which effectively confirmed when the internal cavity was reduced to a certain size, the light absorption ability of CdS@CoP@SiO_2 ball-in-ball photo-reactor would gradually fade away, and the amount of excited charge carriers would significantly reduced. Next, we continue to discuss that the effect of reagent enrichment on the photo-induced activity of CSC-1. Under visible light irradiation, the excited electrons and holes were firstly motivated to the CdS surface, and the electrons were inclined to gather at CoP NPs interface because it has lower potential of conduction band (Fig 11a), reinforcing the separation of charges. And with the photo-induced reaction beginning, the reagent pass through the outer shell enters into the inner cavity depending on concentration difference [3, 16], the hydrogen ions surrounding active sites are constantly consumed instead of being occupied by hydrogen molecules, and owing to narrow inner cavity and the thickest outer shell of CSC-1 that resulting in the exchange hydrogen ions and hydrogen molecules is not smooth. It deserves further explanation, plenty of hydrogen molecules are occupied the sites of the hydrogen ions that directly decreases the probability of reagents contacted with the active site. Thus it caused the most of inner cavity was filled with hydrogen molecules not hydrogen ions during this relaxation time. This phenomenon primarily leads to a large number of hydrogen molecules are trapped inside the cavity in the process of solar-driven activity and leading the inside reagent concentration is lower than outside. Particularly, the experimental data of CS-1 perfectly matches the above phenomenon. As a consequence, the lower reagent concentration and the weaker multi-scattering effect jointly weaken its photocatalytic activity.

With respect to CSC-3, the multi-scattering effect is markedly enhanced compared with CdS@CoP and CSC-1 in the visible-light region (Fig 7a), which can highlight the size of inner cavity would be as the predominant factor of scattering effect. However, due to its largest confined space and the thinnest shell, CSC-3 has the shortest relaxation time and minimum mass transfer resistance so that the exchanging of hydrogen ions and molecules becomes smoother. Thus reagent enrichment effect gradually weakens in CSC-3 ball in ball photo-reactor. And the similar phenomenon in photocatalytic NO removal reaction can be found, the exchanging of reagent molecules becomes easier, which weakened the of reagent enrichment effect. As a further extension, the CS-3 also absolutely confirmed the above theory in the system of photo-reactor without co-catalyst. Thus both CSC-3 and CS-3 show the better HER activity than CSC-1 and CS-1 in the photo-reactor samples.

Up to this point, only the optimized sample CSC-2 is left to discuss. According to the UV-vis spectra, the light absorption of 490-620 nm is stronger than other series of samples, which proved suitable inner cavity is indeed a key factor to enhance the multi-scattering effect. This result renders that CSC-2 presents the highest photocurrent density among these samples, and the suitable hollow structure means it has the lower mass transfer resistance and appropriated inner void, which is beneficial for shortening relaxation time, thereby the exchange of ions and molecules becomes more smooth. In other word, the photo-generated H_2 molecules can exchange with the outside hydrogen ions more easily rather than gather between hydrogen ions and active sites. And then this particular spatial cavity also is positive to enrich the reactive reagent (hydrogen ions) inside the cavity. The above analysis can be evident from in situ IR spectra of NO adsorption in Fig 10, the intensity of several characteristic peaks of CSC-2 was higher than that of CdS@CoP. And referring to NO removal mechanism (Fig 11b), the NO and O_2 molecules passed through outer shell and absorbed around the active core. The inner cavity can provide a stable environment and gradually caused different reagent concentration to promote the redox reaction. In the meanwhile, it is exciting that CS-2 with the similar spatial cavity size also proofs the mechanism again. Based on the above analysis, on account of the higher light absorption and stronger reagent enrichment effect, the CSC-2 exhibits a superior hydrogen production activity among all the as-formed samples [41,42].

According to above experimental data and results, it is confident to draw a conclusion that the suitable size of interior cavity for CdS@CoP@SiO_2 ball-in-ball photo-reactor exactly results in the improvement of multi-scattering effect as well as reagent enrichment effect. It is considering that, notably, these two scientific aspects with their synergistic action promote the enhancement of hydrogen production activity of the obtained photo-reactor samples.

Conclusion

To sum up, we rationally employed the hydrothermal method and modified Stöber method to synthesis the series of CdS@CoP@SiO_2 ball-in-ball nanoreactors with different volumes of interior cavity. More significantly, the CSC-2 exhibits superior visible-light photocatalytic activity than other as-synthesized samples. This result contributes to its suitable interior cavity not only enhances the visible light absorption and reagent enrichment concentration, but also reduces negative impact of mass transfer resistance during the solar-driven hydrogen production process. For comparison, we also fabricate series of CdS@SiO_2 nanoreactors to further verify the effects of spatial cavity on the advanced photo-reactor. As is evident from the various experimental data and analysis, we can confidently highlight that only designing a suitable size of inner cavity can take full advantages of this novel structure for the significantly enhancing HER activity under visible light irradiation. This work can provide a new insight for designing the versatile nature of this novel nanostructure applied in other fields.

Acknowledgement

This work was financially supported by the Natural Science Basic Research Plan in Shaanxi Province of China (Grant No. 2017JZ001), the National Natural Science Foundation of China (Grant No. 21303130), State Key Laboratory of Heavy Oil Processing (SKLOP201602001), the Fundamental Research Funds for the Central Universities (Grant No. cxtd2017004) and K. C. Wong Education Foundation, Hong Kong, China. Thanks for the technical support from International Center for Dielectric Research (ICDR), Xi’an Jiaotong University, Xi’an, China; the authors also appreciate Ms. Dai and Mr. Ma for their help in using SEM, EDX and TEM, respectively.

References

[1] J. Liu, S.Z. Qiao, J.S. Chen, X.W. Lou, X. Xing, G.Q. Lu, Chem. Commun. 47 (2011) 12578-12591.

[2] J.C. Park, J.U. Bang, J. Lee, C.H. Ko, H. Song, J. Mater. Chem. 20 (2010) 1239-1246.

[3] L. Shen, H. Song, G. Yang, C. Wang, ACS Appl. Mater. Interfaces 7 (2015) 11063-11068.

[4] S. Chen, T. Takata, K. Domen, Nat. Rev. Mater. 2 (2017) 17050.

[5] S.H. Choi, Y.C. Kang, ACS Appl. Mater. Interfaces 6 (2014) 2312-2316.

[6] C. Dai, A. Zhang, M. Liu, L. Gu, X. Guo, C. Song, ACS Nano 10 (2016) 7401-7408.

[7] J.C. Park, E. Heo, A. Kim, M. Kim, K.H. Park, H. Song, J. Phys. Chem. C. 115 (2011) 15772-15777.

[8] L. Shen, L. Yu, H.B. Wu, X.Y. Yu, X. Zhang, X.W. Lou, Nat. Commun. 6 (2015) 6694.

[9] V. Subramanian, K. Cheng, C. Lancelot, S. Heyte, S. Paul, S. Moldovan, O. Ersen, M. Marinova, V.V. Ordomsky, A.Y. Khodakov, ACS Catal. 6 (2016) 1785-1792.

[10]L. Zhang, T. Wang, L. Yang, C. Liu, C. Wang, H. Liu, Y.A. Wang, Z. Su, Chemistry 18 (2012) 12512-12521.

[11] T. Zhang, Y. Zuo, M. Liu, C. Song, X. Guo, ACS Omega 1 (2016) 1034-1040.

[12] X. Shi, Z. Lou, P. Zhang, M. Fujitsuka, T. Majima, ACS Appl. Mater. Interfaces 8 (2016) 31738-31745.

[13] W. Zhao, H. Chen, Y. Li, L. Li, M. Lang, J. Shi, Adv. Funct. Mater. 18 (2008) 2780-2788.
[14] X. Fang, X. Zhao, W. Fang, C. Chen, N. Zheng, Nanoscale 5 (2013) 2205-2218.
[15] J. Lee, S.H. Hwang, J. Yun, J. Jang, ACS Appl. Mater. Interfaces 2014, pp. 15420-15426.
[16] B. Lin, S. Chen, F. Dong, G. Yang, Nanoscale 9 (2017) 5273-5279.
[17] Y. Chen, H. Chen, L. Guo, Q. He, F. Chen, J. Zhou, J. Feng, J. Shi, ACS Nano 4 (2010), 529-539.
[18] S.H. Joo, J.Y. Park, C.K. Tsung, Y. Yamada, P. Yang, G.A. Somorjai, Nat. Mater. 8 (2009) 126-131.
[19] Y. Zhao, L. Jiang, Adv. Mater. 21 (2009) 3621-3638.
[20] Q. Zhang, I. Lee, J.B. Joo, F. Zaera, Y. Yin, Acc. Chem. Res. 46 (2013) 1816-1824.
[21] B. Yu, H. Cong, Y. Wang, H. Yuan, L. Xue, R. Yang, Colloid. Polym. Sci. 293 (2014) 985-991.
[22] Q. Zhang, J. Ge, J. Goebl, Y. Hu, Z. Lu,Y. Yin, Nano. Res. 2 (2009) 583-591.
[23] Y. Hu, Q. Zhang, J. Goebl, T. Zhang, Y. Yin, Phys. Chem. Chem. Phys. 12 (2010) 11836-11842.
[24] G. Zhang, L. Yu, H.B. Wu, H.E. Hoster, X.W. Lou, Adv. Mater. 24 (2012) 4609-4613.
[25] Q. Zhang, J. Ge, J. Goebl, Y. Hu, Z. Lu, Y. Yin, Nano. Res. 2 (2010) 583-591.
[26] D. Gross, I. Mora-Seró, T. Dittrich, A. Belaidi,C. Mauser,A.J. Houtepen, D.E. Como, A.L. Rogach, J. Feldmann, J. Am. Chem. Soc. 132 (2010) 5981.
[27] J. Jiang, X. Zhang, P. Sun, L. Zhang, J. Phys. Chem. C. 115 (2011) 20555-20564.
[28] B. Lin, H. Li, H. An, W. Hao, J. Wei, Y. Dai, C. Ma, G. Yang, Appl. Catal. B: Environ. 220 (2018) 542-552.
[29] C. Xue, H. An, X. Yan, J. Li, B. Yang, J. Wei, G. Yang, Nano Energy 39 (2017) 513-523.
[30] C. Xue, X. Yan, H. An, H. Li, J. Wei, G. Yang, Appl. Catal. B: Environ. 222 (2018) 157-166.
[31] C.C. Hou, S. Cao, W.F. Fu, Y. Chen, ACS appl. Mater. Interfaces 7 (2015) 28412-28419.
[32] P. Wang, T. Wu, C. Wang, J. Hou, J. Qian, Y. Ao, ACS Sustain. Chem. Eng. 5 (2017) 7670-7677.
[33] Y. Hu, Y. Liu, H. Qian, Z. Li, J. Chen, Langmuir 26 (2010) 18570-18575.
[34] M. Xing, B. Qiu, M. Du, Q. Zhu, L. Wang, J. Zhang, Adv. Funct. Mater. 27 (2017) 1702624.
[35] X.L. Yin, L.L. Li, W.J. Jiang, Y. Zhang, X. Zhang, L.J. Wan, J.S. Hu, ACS Appl. Mater. Interfaces 8 (2016) 15258-15266.
[36] K. Cheng, Y.P. He, Y.M. Miao, B.S. Zou, Y.G. Wang, T.H. Wang, X.T. Zhang, Z.L. Du, J. Phys. Chem. B 110 (2006) 7259-7264.
[37] K. Hadjiivanov, V. Avreyska, D. Klissurski,T. Marinova, Langmuir 18 (2002) 1619-1625.
[38] J. Wu, Y. Cheng, J. Catal. 237 (2006) 393-404.
[39] R.V. Mikhaylov, A.A. Lisachenko, B.N. Shelimov, V.B. Kazansky, G. Martra, G. Alberto,S. Coluccia, J. Phys. Chem. C 113 (2009) 20381-20387.
[40] T. Wang, Y.-c. Zhu, Z.-y. Xu, L.-g. Wu, Y.-y. Wei, T.-n. Chen, B.-q. Jiang, J. Phys. Chem. C 120 (2016) 12293-12304.
[41]I.Khan, A. Qurashi, G. Berdiyorov, N. Iqbal,K. Fuji,Z.H. Yamani, Nano Energy 44 (2018) 23-33.
[42] X. Liu, W. Xi, C. Li, X. Li, J. Li, Y. Shen, J. He, L. Zhang, L. Xie, X. Sun, P. Wang, J. L, L.-M. Liu, Y. Ding, Nano Energy 44 (2018) 371-377.

Highlights

- Size-controllable CdS@CoP@SiO_2 ball-in-ball photoreactor is firstly obtained.
- The as-prepared photoreactor shows the leading HER activity.
- The effect of interior cavity in the photoreactor on its photoactivity is explored.
- The mechanism of charge transfer in CdS@CoP@SiO_2 is proposed.